

Anomalous electron-phonon coupling in the Kagome ferromagnetic Weyl semimetal $\text{Co}_3\text{Sn}_2\text{S}_2$

G. He,^{1,2,*} M. Kute,^{3,4,*} Z. C. Xu,^{5,6} L. Peis,^{1,7,8,†} R. Stumberger,^{1,7,‡} A. Baum,^{1,7,§} D. Jost,^{1,7,4}
E. M. Been,^{4,9,10} B. Moritz,⁴ Y. G. Shi,^{11,12,¶} T. P. Devereaux,^{3,4,13,**} and R. Hackl^{1,7,8,††}

¹Walther Meissner Institut, Bayerische Akademie der Wissenschaften, Garching 85748, Germany

²Department of Physics, University College Cork, College Road, Cork T12 K8AF, Ireland

³Department of Materials Science and Engineering,
Stanford University, Stanford, California 94305, USA

⁴Stanford Institute for Materials and Energy Sciences,
SLAC National Accelerator Laboratory and Stanford University,
2575 Sand Hill Road, Menlo Park, California 94025, USA

⁵Beijing National Laboratory for Condensed Matter Physics,
Institute of Physics, Chinese Academy of Sciences, Beijing 100190, China

⁶School of Physical Sciences, University of Chinese Academy of Sciences, Beijing 100049, China

⁷School of Natural Sciences, Technische Universität München, Garching 85748, Germany

⁸IFW Dresden, Helmholtzstrasse 20, Dresden 01069, Germany

⁹Department of Physics, Stanford University, Stanford, California 94305, USA

¹⁰Physical Sciences Division, College of Letters and Science,
University of California Los Angeles, Los Angeles, California 90095, USA

¹¹Beijing National Laboratory for Condensed Matter Physics,
Institute of Physics, Chinese Academy of Sciences, Beijing 100190, China.

¹²Songshan Lake Materials Laboratory, Dongguan, Guangdong 523808, China

¹³Geballe Laboratory for Advanced Materials, Stanford University, Stanford, California 94305, USA

(Dated: January 29, 2024)

We present results of a Raman scattering study of the Kagome ferromagnet $\text{Co}_3\text{Sn}_2\text{S}_2$, with a focus on electronic and phononic excitations and their interplay. In addition, the electronic band structure is analyzed theoretically, enabling a semi-quantitative explanation of the spectra. A prominent feature in the electronic spectra is a redistribution of spectral weight from low to high energies starting at the Curie temperature T_C . The Raman intensity is suppressed below approximately 1000 cm^{-1} and increases above to a peak at 2000 cm^{-1} in all symmetries. Two Raman active phonon modes are identified in A_{1g} and E_g symmetry. The A_{1g} phonon couples strongly to the electronic continuum as indicated by the asymmetric Fano-type line shape. The asymmetry depends non-monotonically on temperature and is maximal close to the magnetic transition. In the limit $T \rightarrow 0$ the phonon is nearly symmetric. The evolution of the coupling strength and the electronic continuum as a function of temperature is attributed to a band splitting induced by the ferromagnetic phase transition which substantially reduces the DOS towards $T = 0$. The $3d_{z^2}$ electrons of the Co atoms in the crystal field modulated by the A_{1g} phonon are implied to be a critical component contributing to the strong electron-phonon coupling of that phonon. These results allow a comprehensive understanding of the bulk band structure evolution as a function of temperature in $\text{Co}_3\text{Sn}_2\text{S}_2$, offering key insights for further studies of the driving force behind the long-range magnetic order and novel topological states in this compound.

I. INTRODUCTION

Materials stacked with a Kagome lattice present rich fundamental physics - such as frustrated magnetism, topological quantum electronic states, electronic correlation and superconductivity - that have received increased attention in recent years¹⁻⁵. Among them, the Kagome magnet $\text{Co}_3\text{Sn}_2\text{S}_2$ is one of the ideal prototypes, possessing intrinsic ferromagnetism and a nontrivial topological state⁶⁻⁹. The magnetic Co atoms in $\text{Co}_3\text{Sn}_2\text{S}_2$ form a Kagome lattice in the ab -plane as seen in Fig. 1 (a). It shows an out-of plane ferromagnetic phase transition at the Curie temperature $T_C \sim 177 \text{ K}$ with magnetic moment of $0.3 \mu_B/\text{Co}$ ¹⁰.

$\text{Co}_3\text{Sn}_2\text{S}_2$ is an ideal candidate for studying magnetic Weyl semimetals, evidenced by the intrinsically large

anomalous Hall effect^{8,9}, the zero-field Nernst effect¹¹ and surface Fermi arcs observed by scanning tunneling microscopy (STM) and angle-resolved photoemission spectroscopy (ARPES)^{6,7}. The underlying electron correlations¹² and flat bands^{12,13} make this system interesting in a general context. Furthermore, both infrared^{12,14} and magneto-optic Kerr effect¹⁵ measurements disclosed a spectral weight redistribution below T_C , which was explained as a temperature-induced band shift by Yang *et al.*¹⁴. In spite of the quasi-quantitative match between the density functional theory (DFT) calculations and experimental results^{14,16}, the driving force of the long-range magnetic order is still elusive.

While this material in many ways resembles itinerant Stoner ferromagnetism¹⁷, the magnetic interactions and related ground states in $\text{Co}_3\text{Sn}_2\text{S}_2$ are subtle. Along with

the ferromagnetic phase transition, an in-plane antiferromagnetic (AFM) order above 90 K was revealed by muon-spin relaxation/rotation (μ SR)¹⁸, whereas recent neutron scattering measurements dispute the claims of the in-plane AFM between 90 K and T_C ¹⁹.

Probing the low-energy excitations in $\text{Co}_3\text{Sn}_2\text{S}_2$ can at least partially uncover the electronic structure near the Fermi level. Among the various excitations, phonons and the underlying electron-phonon coupling (EPC) can provide deep insights about the low energy electronic structure. Vibrational spectroscopies like Raman and infrared play a crucial role in exploring the phonons at the Γ point and the related EPC^{20–25}. The interference between the discrete phonon and continuous electronic states leads to an asymmetric so-called Breit-Wigner-Fano line shape^{26,27}. This Fano resonance is seldom observed in conventional metals due to strong metallic screening. This is not the case for the majority of Dirac or Weyl semimetals, however, in which the band crossing points (Dirac or Weyl points) are near the Fermi level entailing a reduced electronic density of states (DOS) and weaker screening. As a result, strong Fano resonances are widely observed in these materials, e.g. graphene^{28–30}, TaAs²⁵ and LaAlSi³¹. Thus, the desire to obtain in-depth knowledge of the low energy excitations in the topological materials motivates our light scattering study of $\text{Co}_3\text{Sn}_2\text{S}_2$.

In this paper, we present a polarization-dependent Raman study on high-quality single crystals of $\text{Co}_3\text{Sn}_2\text{S}_2$ at temperatures ranging from 14 K to 310 K. Two Raman active phonons were identified. The A_{1g} phonon shows a Fano-type line shape above T_C which disappears gradually below T_C . The E_g phonon has a symmetric Lorentzian line shape in the whole temperature range, indicative of weak electron-phonon coupling. The electronic continuum exhibits a spectral weight redistribution below T_C in both the E_g and the $A_{1g} + A_{2g}$ symmetries with a loss of spectral weight below 1000 cm^{-1} along with an increase for higher energies. The temperature dependence of the A_{1g} phonon and the continuum argue in favor of electron-phonon coupling which is enhanced by modulating the crystal field along the c -axis. As a result, the A_{1g} phonon induces motion of the Weyl points in reciprocal space. The increase of EPC with temperature in the ferromagnetic state is driven by an increase of the DOS toward T_C , suggesting a fundamental link to the Stoner instability. The non-monotonic coupling strength for the A_{1g} phonon and the redistribution of the spectral weight in all symmetries indicate that bands split and shift across T_C . Our results provide key ingredients for further investigation of the ferromagnetic phase transition and novel topological states in $\text{Co}_3\text{Sn}_2\text{S}_2$.

II. METHODS

A. Samples

$\text{Co}_3\text{Sn}_2\text{S}_2$ single crystals are grown by a self-flux method as described in Ref.⁹. The samples were characterized by X-ray diffraction (XRD) and magnetization measurements showing a high crystallinity and a ferromagnetic phase transition at $T_C = 177 \text{ K}$ (See more details in Supplemental Material A).

B. Raman experiments

The experiments were performed with a scanning spectrometer with the resolution set at 4.5 cm^{-1} at 575 nm . Since one of the phonon lines has a width comparable to the resolution a Voigt function (convolution of a Gaussian and a Lorentzian) is used for describing the phonons. For excitation a solid-state laser emitting at 575 nm (Coherent GENESIS MX-SLM577-500) was used hitting the sample at an angle of incidence of 66° . Several experiments were performed with the green (514 nm) and violet (458 nm) lines of an Ar laser. The incoming light was polarized outside the cryostat in a way that the polarization inside the sample had the desired components. The sample was mounted with good thermal contact to the cold finger of a ^4He -flow cryostat with the surface normal parallel to the optical axis of the spectrometer. The local heating by the laser was determined to be approximately 1 K/mW absorbed power P_a . For most of the experiments P_a was set at 2 mW . The vacuum was better than 10^{-6} mbar .

The Raman susceptibilities shown in the figures, $R\chi''(\Omega, T)$, are equal to the dynamical structure factor $S(\Omega, T)$ divided by the Bose-Einstein distribution function $\{1 + n(\Omega, T)\}$, where R is an experimental constant, and $S(\Omega, T)$ is proportional to the rate of scattered photons³². Since $\text{Co}_3\text{Sn}_2\text{S}_2$ has a hexagonal lattice (point group D_{3d}) as shown in Fig. 1 (a) circular polarizations are convenient and were used in most of the experiments. $\hat{R}\hat{R}$ ($\hat{R}\hat{L}$) means that incoming and outgoing photons were both right-circularly (right- and left-circularly) polarized etc., where $\hat{R}, \hat{L} = \hat{x} \pm i\hat{y}$ with the perpendicular linear polarizations \hat{x} and \hat{y} . The position of the atoms and related space group ($R\bar{3}m$) of $\text{Co}_3\text{Sn}_2\text{S}_2$ entail the existence of two Raman active modes having A_{1g} and E_g symmetry. They appear in the spectra measured with $\hat{R}\hat{R}$ and $\hat{R}\hat{L}$ polarization configurations, respectively, in the Kagome Co_3Sn plane as shown in Fig. 1 (b) and (e). In addition A_{1g} symmetry, A_{2g} excitations are projected in $\hat{R}\hat{R}$ configuration and may be relevant for the electronic or spin response.

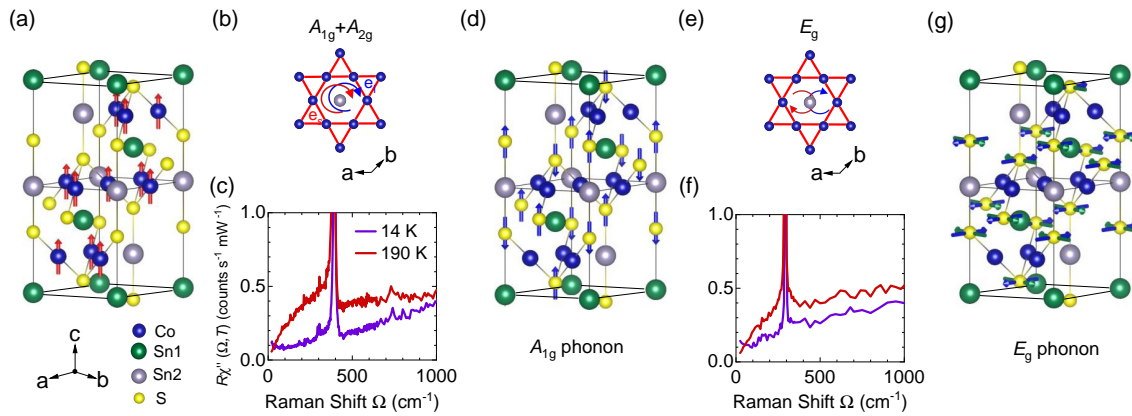


Figure 1. **Crystal structure and Raman active phonon modes of $\text{Co}_3\text{Sn}_2\text{S}_2$.** (a) Crystal structure of $\text{Co}_3\text{Sn}_2\text{S}_2$. The red arrows on the Co atoms indicate the spin orientation in ferromagnetic state. (b) and (e) Polarization configurations used in the Raman measurements. Based on the Raman selection rule in the $\text{Co}_3\text{Sn}_2\text{S}_2$ lattice, the right-right and right-left polarization configurations in the Co_3Sn layer project out the $A_{1g} + A_{2g}$ and the E_g symmetries, respectively. (d) and (g) Eigenvectors of A_{1g} and E_g phonons, respectively. The A_{1g} and E_g phonons only involve S atom vibrations either out-of-plane (A_{1g}) or in-plane (E_g). Note that the E_g phonon is doubly degenerate, with two orthogonal vibration modes [green and blue arrows in (g)]. (c) and (f) The Raman spectra at 14 K and 190 K in the $A_{1g} + A_{2g}$ and the E_g symmetries, respectively.

C. DFT calculations

Electronic and phonon properties were calculated using DFT as implemented in the Vienna Ab Initio Simulation Package (VASP)^{33,34}, using projector augmented wave (PAW) pseudo-potentials, the Perdew-Burke-Ernzerhof (PBE) functional³⁵, and an energy cutoff of 500 eV. Self-consistent field calculations were performed on a $7 \times 7 \times 7$ \mathbf{k} -point grid, which was increased to $39 \times 39 \times 39$ for density of states calculations and reduced to $3 \times 3 \times 3$ for phonon supercell calculations. The structures were relaxed independently for the ferromagnetic and paramagnetic phases such that the forces on atoms were less than 10^{-7} eV/Å. The phonon energies and eigenvectors were calculated using the Phonopy package^{36,37}. Raman-active phonons were identified at the Γ point corresponding to the A_{1g} and E_g phonons found experimentally.

The electron-phonon coupling (EPC) for the Raman-active phonons was estimated using the frozen phonon method³⁸. Atoms were displaced by 0.05 Å along the phonon eigenvectors, and the electron-phonon matrix element was calculated as follows,

$$g_{i,\lambda}(k) = \sqrt{\frac{\hbar}{2m_S\omega}} \frac{\partial E_i}{\partial x} \quad (1)$$

where i is the band index, λ is the phonon index, m_S is the mass of sulfur, the only moving atom in this case, ω is the phonon angular frequency, and $\partial E/\partial x$ is the change in band energy from the unperturbed case, divided by the displacement. From this, we are able to calculate the overall EPC strength constant as

$$\lambda_{\text{EPC}} = \frac{N_F g^2}{\hbar\omega} \quad (2)$$

where N_F is the density of states at the Fermi level for

both spins, and g is the EPC matrix element averaged over the Fermi level²¹.

III. RESULTS

A. Phonons

As an overview, the $A_{1g} + A_{2g}$ and the E_g Raman responses below and above T_C are shown in Fig. 1 (c) and (f). The E_g phonon line (in-plane vibration of S atoms [(Fig. 1 (g))]) is almost symmetric, whereas the A_{1g} phonon (out of plane vibration of S atoms [Fig. 1 (d)]) is obviously asymmetric above and around T_C , consistent with previous Raman results³⁹. Both phonons are superposed on temperature dependent electronic continua.

Figure 2 displays the experimental results for the phonons in $\text{Co}_3\text{Sn}_2\text{S}_2$ at temperatures as indicated. The A_{1g} phonon [Fig. 2 (a)] is asymmetric, particularly in the temperature range around the ferromagnetic transition. In the limit $T \rightarrow 0$ the line becomes nearly symmetric. Since the line width Γ is much smaller than the resonance energy ω_{ph} the usual (simplified) expression for the Fano resonance valid close to ω_{ph} ,

$$A(\omega) = \frac{A_0}{|q^2 + 1|} \frac{(q + \varepsilon)^2}{1 + \varepsilon^2} + c(\omega); \quad \varepsilon = 2 \frac{\omega - \omega_{\text{ph}}}{\Gamma}, \quad (3)$$

can be used to extract the asymmetry parameter q which describes the coupling between the harmonic phonon oscillator and the continuous electronic excitations $c(\omega)$. For $|q| \rightarrow \infty$ or, equivalently, $1/|q| \rightarrow 0$, a Lorentzian phonon line is recovered. A_0 is the oscillator strength of the phonon. For modeling $c(\omega)$ a phenomenological expression is used. The analysis of the phonon line in the

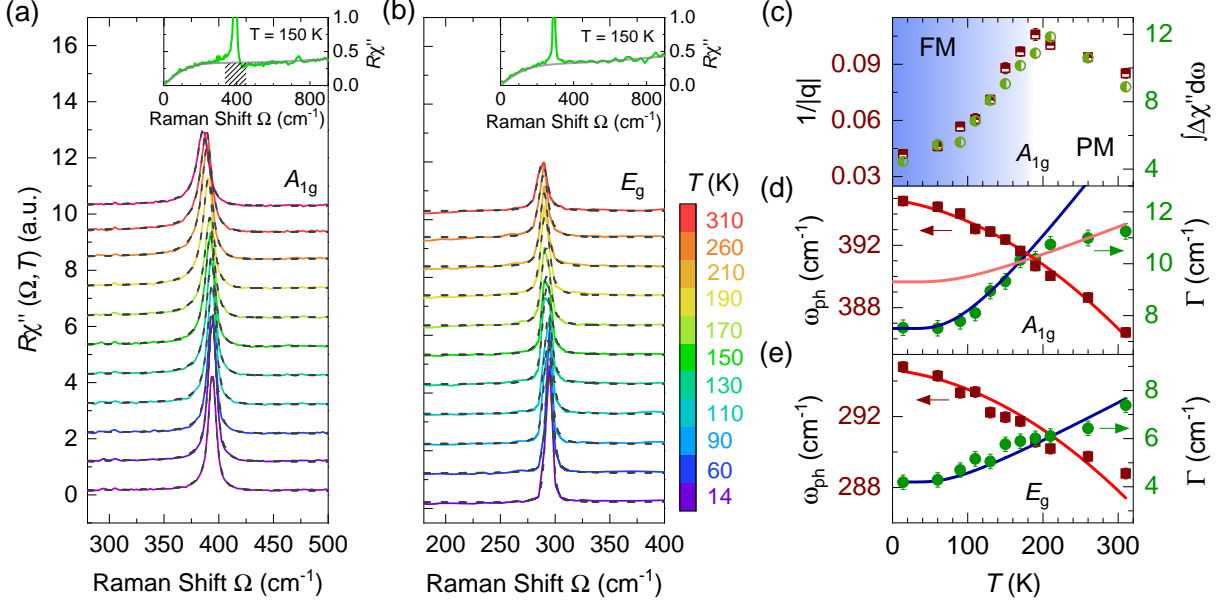


Figure 2. **Raman-active phonon modes in $\text{Co}_3\text{Sn}_2\text{S}_2$.** (a) and (b) Experimental results for the A_{1g} and the E_g phonon lines at temperatures as indicated by the color bar. The solid and dashed lines represent the experimental data and theoretical curves, respectively. The data are shifted vertically for clarity. The A_{1g} phonon line is best represented by a Fano function. The symmetric E_g phonon line is described by a Voigt function. Insets in (a) and (b): The continuum is described by a smooth phenomenological curve (gray line). (c) Temperature dependence of the inverse asymmetry factor $1/|q|$ of the A_{1g} phonon extracted from the fits (half filled red squares) and area of the electronic continuum integrated in the range $\omega_{ph}^{A_{1g}} \pm 50 \text{ cm}^{-1}$ (hatched area in (a), half filled green circles). (d) and (e) Temperature dependencies of phonon resonance energies ω_{ph} and linewidths Γ . The solid curves are derived from the volume expansion using Grüneisen theory for the phonon energies and the anharmonic decay model for the linewidths, respectively [see Suppl. Material B]. Different phonon-phonon coupling parameters λ_{ph-ph} are used for describing the linewidths of the A_{1g} phonon separately below (blue curve) and above (orange curve) T_C .

entire temperature range yields a strong variation of the asymmetry parameter $1/|q|$ peaking at 190 K and a rapid reduction of the line width $\Gamma^{A_{1g}}$ below T_C [Fig. 2 (c) and (d)]. The crossover of $\Gamma^{A_{1g}}(T)$ at T_C is apparently related to the anomaly the found for $1/|q|$. The spectral weight of the continuum in the range $\omega_{ph} \pm 50 \text{ cm}^{-1}$ varies in a similar fashion as the parameter $1/|q|$ indicating a direct interrelation of the continuum and the phonon (half filled green circles in Fig. 2(c)). The spectral weight of the continuum will be addressed in detail in section III B.

The energy and the linewidth of the E_g phonon does not exhibit unusual variations with temperature and may be described in terms of the thermal expansion according to the Grüneisen theory and the anharmonic decay, respectively [Fig. 2(b) and (e)]. The details of determining the related parameters are summarized in Supplemental Material B. The energies, linewidths, phonon-phonon coupling constants and the Grüneisen constants for both phonons are listed in Table I.

B. Electronic excitations

The temperature-dependent Raman responses at high energies in $\hat{R}\hat{R}$ and $\hat{R}\hat{L}$ polarization configurations are

Table I. **Phonon parameters of $\text{Co}_3\text{Sn}_2\text{S}_2$.** The experimental energies ω_{ph} and widths (Γ) of the Raman-active phonons are measured at 14 K. The Grüneisen constants γ_i are obtained from comparing the volume expansion and the temperature dependent phonon energies ω_{ph} ⁴⁰. The phonon-phonon coupling parameters $\lambda_{i,ph-ph}$ are derived from an anharmonic model for symmetric decay⁴¹. Different phonon-phonon coupling parameters λ_{ph-ph} are used for describing the linewidths of the A_{1g} phonon below (blue curve) and above (orange curve) T_C . The phonon energies and electron-phonon coupling constants $\lambda_{i,el-ph}$ derived from the simulations are also listed.

Phonon		A_{1g}	E_g
ω_{ph} (cm^{-1})	Simulation (FM)	400.1	298.8
	Experiment	394.8	294.8
Γ (cm^{-1})		7.5	4.2
γ_i		2.18	2.82
$\lambda_{i,ph-ph}$	FM	0.75	0.42
	PM	0.18	
$\lambda_{i,el-ph}$ (Simulation)	FM	0.030	0.019
	PM	0.048	0.027

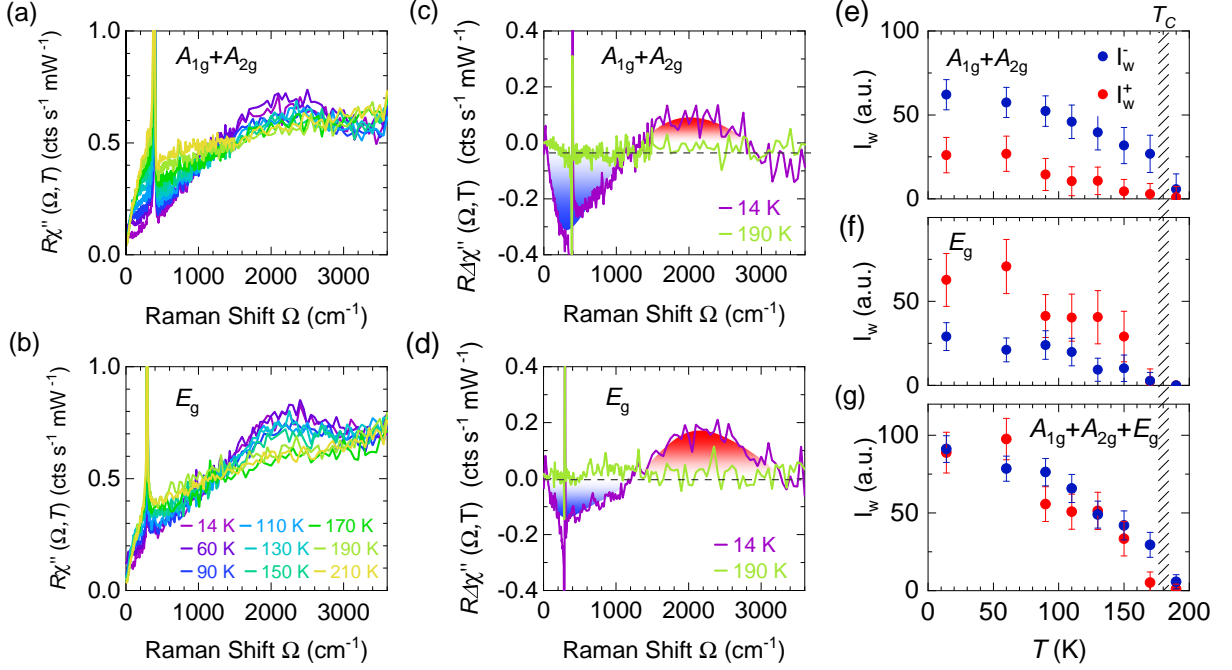


Figure 3. **Temperature-dependent electronic Raman response of $\text{Co}_3\text{Sn}_2\text{S}_2$.** Raman spectra in (a) $A_{1g} + A_{2g}$ and (b) E_g symmetry at various temperatures as indicated. The measurements were performed with the yellow laser ($\lambda_L = 575$ nm). The difference of the spectra between the indicated temperatures and 210 K in the $A_{1g} + A_{2g}$ and the E_g symmetries, respectively. The spectra at 14 K are fitted by a 5-order polynomial in order to show the profile of the spectra. The blue regions and the red regions indicate the negative and positive intensity of the difference spectra respectively. (e), (f), and (g) Temperature dependence of integrated spectral weight in the $A_{1g} + A_{2g}$, E_g , and $A_{1g} + A_{2g} + E_g$ symmetries. The positive (red points) and negative (blue points) intensity regions are integrated separately. The error bars are given by $|\overline{\Delta\chi''} - \overline{\Delta\chi''_{fit}}| \times \Delta\Omega$, where $|\overline{\Delta\chi''} - \overline{\Delta\chi''_{fit}}|$ is defined as the average noise of the difference spectra, $\Delta\Omega$ is the Raman shift range of the positive or negative intensity region. The ferromagnetic phase transition temperature is indicated by the hatched areas.

presented in Fig. 3. In either case, one observes a redistribution of spectral weight from below approximately 1400 cm^{-1} to above when the temperature is reduced below the Curie point T_C . The redistribution of spectral weight is well reproduced for different laser excitations (see Supplemental Material C for details). The $A_{1g} + A_{2g}$ spectra ($\hat{R}\hat{R}$) show a strong reduction of the response and a relatively weak pile-up whereas in the E_g spectra ($\hat{R}\hat{L}$) the redistribution is just the other way around. The strong reduction of the intensity in the \hat{R}, \hat{R} spectra goes along with a decrease of the line width Γ and the asymmetry parameter $1/|q|$ of the A_{1g} phonon as briefly mentioned in section III A. Here, we observe that the intensity is reduced over a range of 1400 cm^{-1} . In the range around the phonon, approximately 70% are lost presumably due to the decrease of the DOS, and it may be expected that the renormalization of the phonon through electron-phonon coupling becomes much weaker. In E_g symmetry, the phonon is largely unaffected, and we conclude that the coupling is negligible.

An additional unexpected aspect is uncovered if the integrals for the low-energy and high-energy parts below and above the intersection points at 1400 cm^{-1} are compared. Since the temperature dependence of the elec-

tronic spectra starts only below 190 K we use the response at 210 K and subtract it from all spectra measured below 210 K (Spectra at higher temperatures can be found in Supplemental Material D). For practical reasons, because the distance of the experimental points varies, we approximate all spectra by fifth-order polynomials. The magnitudes of the reduction and increase are shown in blue and red in panels (c) and (d) of Fig. 3. As opposed to the optical conductivity there is no sum rule for the Raman response^{42,43} and the loss and the gain in spectral weight do not compensate each other but rather follow the trend which can be seen directly in the results. Surprisingly however, if the intensities in the two configurations which in fact include all symmetries accessible for in-plane polarizations are added there is a compensation of loss and gain to within the experimental error [Fig. 3 (g)].

C. Simulations

The band structure of both the FM and PM states of $\text{Co}_3\text{Sn}_2\text{S}_2$ can be found in Fig. 4 (a). The PM band structure [dashed lines in Fig. 4 (a)] has a spin-

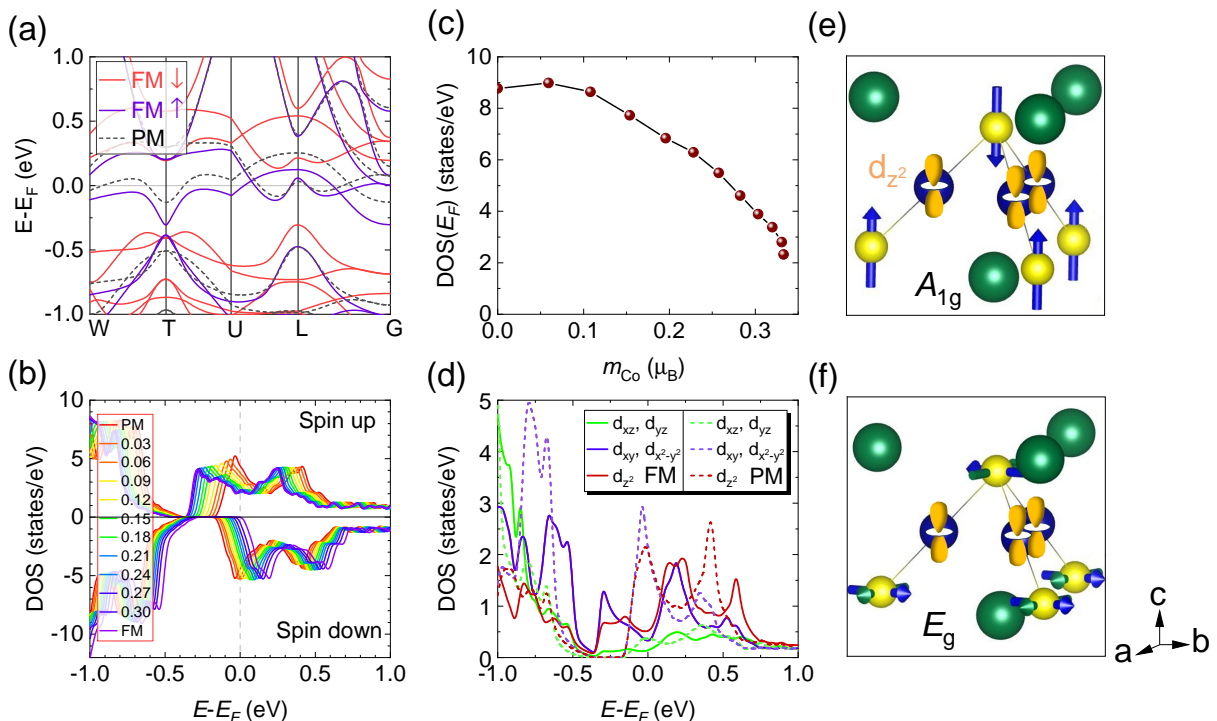


Figure 4. **Electronic structure of $\text{Co}_3\text{Sn}_2\text{S}_2$.** (a) Band structure without spin-orbit coupling for the paramagnetic (PM) (dashes) and ferromagnetic (FM) states (spin-down: red curves, spin-up: purple curves). (b) Density of states (DOS) near the Fermi level (E_F) versus magnetic moments of the Co atom in units of μ_B/Co . The DOS for spin-up and spin-down states are summed up. (c) DOS at E_F as a function of the magnetic moment of the Co atom. (d) Orbital-resolved DOS in the PM state (dashed lines) and the FM state (solid lines). (e) and (f) Schematic of the electron-phonon coupling for A_{1g} and E_g phonons. Cartoons of d_{z^2} orbitals are superimposed on the Co atoms (blue). (e) When the S atoms (yellow) move in and out of the Kagome plane in the case of the A_{1g} phonon the electric field across the d_{z^2} orbitals is modulated. (f) The field does not change when the S atoms move parallel to the plane.

degenerate nearly-flat band near the Fermi level, which splits into two distinct spin channels in the FM ground state [solid lines in Fig. 4 (a)], separated by roughly 300 meV. Indeed, both Weyl bands shift relative to the Fermi level across the phase transition. This band shift may explain the spectral weight redistribution in the Raman spectra seen in Fig. 3.

The results of the phonon calculations are summarized in Table I. The predicted phonon energies are higher than the experimental values by less than 2%. The phonon energies for the PM case only deviate by less than 1% from the FM case and are thus omitted here. The calculations also indicate that the EPC strength is significantly higher for A_{1g} than for E_g , and that both figures are higher for the PM than the FM phase. The large EPC in the PM state explains why the Fano effect of the A_{1g} phonon survives above T_C .

The band response to the phonon displacements can be found in the Supplemental Material E, and it is evident that the A_{1g} phonon elicits a much larger change in the band structure than the E_g in both the PM and FM states. In addition, we observe large phonon-induced band shifts for A_{1g} both in the FM and PM band structures (see Supplemental Material E for details), which in-

dicates that the DOS, rather than band response alone, is driving the increase in EPC strength, as per Eq. 2. Given that the magnetic moment increases as temperature decreases, we use the total magnetization in the simulation as a proxy for temperature and observe that the DOS decreases drastically when moving from the PM to the FM phases [Fig. 4 (b) and (c)]. This explains the monotonic increase of the Fano asymmetry $1/|q|$ below T_C displayed in Fig. 2 (c).

The phonon-induced band response results in a shift of the Weyl points in reciprocal space. A 0.02 \AA shift of the S atoms along the phonon eigenvectors moves the Weyl points by $8.0 \times 10^{-4} \text{ \AA}^{-1}$ and $6.8 \times 10^{-4} \text{ \AA}^{-1}$ for the two degenerate E_g phonons, and by $5.0 \times 10^{-3} \text{ \AA}^{-1}$ for the A_{1g} phonon, nearly an order of magnitude more. Thus the two phonons provide a knob of fine tuning the topological behavior in this material. More details about the motion of the Weyl point can be found in Supplemental Material E.

IV. DISCUSSION

The polarization dependence of the electronic spectra directly indicates the existence of selection rules. According to our understanding, there are no coherence effects in a ferromagnet similar to those in a superconductor. Thus, the intensity redistribution is presumably a result of the reconstruction of the band structure alone. Indeed, spectral weight redistribution has been observed in various experiments, including optical conductivity^{12,14}, magneto-optic Kerr effect¹⁵, and resonant inelastic X-ray scattering⁴⁴. This redistribution is associated with the band shift induced by ferromagnetic phase transition¹⁴, which has been directly observed in recent ARPES measurements⁴⁵.

Our DFT simulations also demonstrate that bands hosting spin-up and spin-down electrons become split. If we assume that we predominantly observe interband transitions, we may conclude that the energy difference of some bands around the Fermi surface increases below 1400 cm^{-1} , quenching transitions available above the phase transition.

Furthermore, the non-monotonic enhancement of EPC in the A_{1g} phonon hints at potential low-lying excitations, possibly originating from either Weyl bands^{7,16} or flat bands^{12,13,44}. Yet, we cannot clarify the actual origin from the Raman experiments and the DFT calculations at this point. The DOS including the effective magnetic moment of the Co atom explains the increased EPC in the PM state, but this dependence alone does not explain why response the of the band structure is larger for the A_{1g} than the E_g phonon. To understand this dichotomy, we look at the eigenvectors.

Essentially, the EPC originates from the electrostatic potential generated by the displacement of the atoms. This phonon-induced potential modulates the electronic behavior. Specifically, the A_{1g} phonon in $\text{Co}_3\text{Sn}_2\text{S}_2$ is a predominantly diametrical vibration of S atoms perpendicular to the Kagome plane [see Fig. 4 (e)]. It induces density fluctuations of the Co d -electrons along the c -axis due to the asymmetric crystal field environment across the Kagome plane. This, in principle, would enhance EPC, in a similar fashion as the B_{1g} phonon in $\text{YBa}_2\text{Cu}_3\text{O}_7$ ²¹. Among the five d orbitals of Co $3d$ electrons, the strictly in-plane d_{xy} and $d_{x^2-y^2}$ orbitals couple weaker to the out-of-plane S motion of the A_{1g} phonon than the d_{xz} , d_{yz} , and d_{z^2} orbitals. Among them, the d_{z^2} orbital dominates the EPC, since it contributes much more to the DOS near the Fermi level than the d_{xz} and d_{yz} orbitals (see Fig. 4 (d) and Supplemental Material F for details). Furthermore, the DOS originating from the d_{z^2} orbital in the PM state is much higher than that in the FM state thus explaining the reduced EPC in the FM state. In contrast, the motion of the S atoms is in plane for the E_g phonon, and the modulation of the electric field across the Kagome plane is negligible (see Fig. 4 (f)). Consequently, the coupling to Co $3d_{z^2}$ electrons is much weaker substantially reducing the band shifts near

the Fermi level. In a similar fashion, the motion of the Weyl points induced by the phonons is almost an order of magnitude larger for the A_{1g} than the E_g phonon.

V. CONCLUSIONS

In summary, we studied the Raman spectra of $\text{Co}_3\text{Sn}_2\text{S}_2$ single crystal as a function of polarization and temperature and analyzed the results theoretically. The electronic continua in the range up to 3600 cm^{-1} in both polarization configurations, $\hat{R}\hat{R}$ ($A_{1g} + A_{2g}$) and $\hat{R}\hat{L}$ ($E_g^{(1)}$ and $E_g^{(2)}$), show a redistribution of spectral weight below T_C from below 1400 cm^{-1} to above. The piled-up intensity peaks at approximately 2000 cm^{-1} . Since a ferromagnet does not exhibit gap-like structures in a single band but rather a shift of the spin-up and spin-down bands with respect to the Fermi energy we conclude that the redistribution of intensity below T_C originates predominantly from band shifts.

Both Raman-active phonon modes were identified to have A_{1g} and E_g symmetry. The E_g mode has a conventional Lorentzian shape. The A_{1g} phonon exhibits an asymmetric Fano-type line shape, indicative of strong coupling to the electronic continuum. The asymmetry factor $1/|q|$ varies non-monotonically with temperature and increases upon approaching T_C from below and decreases again above. $1/|q|(T)$ follows closely the variation of the intensity of the electronic continuum thus supporting the hypothesis of enhanced EPC in $\text{Co}_3\text{Sn}_2\text{S}_2$. The DFT simulations show that the EPC scales with the electronic density of states further supporting the coupling hypothesis. Predominantly the d_{z^2} orbital of Co $3d$ electrons is involved in the EPC of the A_{1g} phonon through the crystal field gradient along the c -axis. These results indicate an evolution of electronic structure as a function of temperature along with the magnetic moment. The analysis of the electron-phonon coupling highlights the importance of the d_{z^2} orbital for the low energy excitations in $\text{Co}_3\text{Sn}_2\text{S}_2$. The shift of the Weyl points and the interrelation of temperature and magnetization suggested by the analysis of the A_{1g} phonon argues for an intriguing entanglement of lattice structure, magnetic order and topology in $\text{Co}_3\text{Sn}_2\text{S}_2$.

Acknowledgments

We thank C.-J. Yi, R. Yang, D.-F. Liu, Y.-F. Xu, Y.-T. Sheng, Z.-D. Song for fruitful discussions. This work is supported by the Deutsche Forschungsgemeinschaft (DFG) through the coordinated programme TRR80 (Projekt-ID 107745057) and projects HA2071/12-1 and -3. L.P. and R.H. were partially supported by the Bavaria-California Technology Center (BaCaTeC) under grant number A3 [2022-2]. G.H. would like to thank the Alexander von Humboldt Foundation for a research fellowship. D.J. gratefully acknowledges funding of the Alexander von Humboldt foundation via

a Feodor Lynen postdoctoral fellowship. The work for sample synthesis and characterization was supported by grants from the Informatization Plan of the Chinese Academy of Sciences (CAS-WX2021SF-0102), and the Synergetic Extreme Condition User Facility (SECUF). Work at SLAC National Accelerator Laboratory and Stanford University (M.K., D.J., E.M.B., B.M., T.P.D.) was supported by the U.S. Department of Energy, Office of Basic Energy Sciences, Division of Materials Sciences and Engineering, under Contract No. DE-AC02-76SF00515. The computational results utilized the resources of the National Energy Research Scientific Computing Center (NERSC) supported by the U.S. Department of Energy, Office of Science, under Contract

No. DE-AC02-05CH11231.

Author contributions

G.H. and R.H. conceived the project. G.H., L. P., R.S., A.B. and D.J. performed the Raman measurements. G.H., M.K., L.P., T.P.D., and R.H. analysed the Raman data. Z.C.X. and Y.G.S. synthesised and characterised the samples. M.K., E.M.B., B.M. and T.P.D. performed DFT calculations. G.H., M.K. and R.H. wrote the manuscript with comments from all the authors.

Competing interests

The authors declare no competing interests.

* These authors contributed equally to the work.

† Present address: Capgemini, Frankfurter Ring 81, 80807 München, Germany

‡ Present address: Robert Bosch GmbH, Robert-Bosch-Campus 1, 71272 Renningen, Germany

§ Present address: Mynaric, Bertha-Kipfmüller-Str. 2-4, 81249 München, Germany

¶ Corresponding author: ygshi@iphy.ac.cn

** Corresponding author: tpd@stanford.edu

†† Corresponding author: hackl@tum.de

¹ B. Normand, *Contemporary Phys.* **50**, 533 (2009).

² M. Kang, S. Fang, L. Ye, H. C. Po, J. Denlinger, C. Jozwiak, A. Bostwick, E. Rotenberg, E. Kaxiras, J. G. Checkelsky, and R. Comin, *Nat. Commun.* **11**, 4004 (2020).

³ J.-X. Yin, S. S. Zhang, H. Li, K. Jiang, G. Chang, B. Zhang, B. Lian, C. Xiang, I. Belopolski, H. Zheng, T. A. Cochran, S.-Y. Xu, G. Bian, K. Liu, T.-R. Chang, H. Lin, Z.-Y. Lu, Z. Wang, S. Jia, W. Wenhong, and M. Z. Hasan, *Nature* **562**, 91 (2018).

⁴ J.-X. Yin, W. Ma, T. A. Cochran, X. Xu, S. S. Zhang, H.-J. Tien, N. Shumiya, G. Cheng, K. Jiang, B. Lian, Z. Song, G. Chang, I. Belopolski, D. Multer, M. Litskevich, Z.-J. Cheng, X. P. Yang, B. Swidler, H. Zhou, H. Lin, T. Neupert, Z. Wang, N. Yao, T.-R. Chang, S. Jia, and M. Zahid Hasan, *Nature* **583**, 533 (2020).

⁵ B. R. Ortiz, S. M. L. Teicher, Y. Hu, J. L. Zuo, P. M. Sarte, E. C. Schueller, A. M. M. Abeykoon, M. J. Krogstad, S. Rosenkranz, R. Osborn, R. Seshadri, L. Balents, J. He, and S. D. Wilson, *Phys. Rev. Lett.* **125**, 247002 (2020).

⁶ N. Morali, R. Batabyal, P. K. Nag, E. Liu, Q. Xu, Y. Sun, B. Yan, C. Felser, N. Avraham, and H. Beidenkopf, *Science* **365**, 1286 (2019).

⁷ D. F. Liu, A. J. Liang, E. K. Liu, Q. N. Xu, Y. W. Li, C. Chen, D. Pei, W. J. Shi, S. K. Mo, P. Dudin, T. Kim, C. Cacho, G. Li, Y. Sun, L. X. Yang, Z. K. Liu, S. S. P. Parkin, C. Felser, and Y. L. Chen, *Science* **365**, 1282 (2019).

⁸ Q. Wang, Y. Xu, R. Lou, Z. Liu, M. Li, Y. Huang, D. Shen, H. Weng, S. Wang, and H. Lei, *Nat. Commun.* **9**, 3681 (2018).

⁹ E. K. Liu, Y. Sun, N. Kumar, L. Muechler, A. L. Sun, L. Jiao, S. Y. Yang, D. F. Liu, A. J. Liang, Q. N. Xu,

J. Kroder, V. Suss, H. Borrmann, C. Shekhar, Z. S. Wang, C. Y. Xi, W. H. Wang, W. Schnelle, S. Wirth, Y. L. Chen, S. T. B. Goennenwein, and C. Felser, *Nat. Phys.* **14**, 1125 (2018).

¹⁰ P. Vaqueiro and G. G. Sobany, *Solid State Sci.* **11**, 513 (2009).

¹¹ S. N. Guin, P. Vir, Y. Zhang, N. Kumar, S. J. Watzman, C. G. Fu, E. K. Liu, K. Manna, W. Schnelle, J. Gooth, C. Shekhar, Y. Sun, and C. Felser, *Adv. Mater.* **31**, 1806622 (2019).

¹² Y. Xu, J. Zhao, C. Yi, Q. Wang, Q. Yin, Y. Wang, X. Hu, L. Wang, E. Liu, G. Xu, L. Lu, A. A. Soluyanov, H. Lei, Y. Shi, J. Luo, and Z.-G. Chen, *Nat. Commun.* **11**, 3985 (2020).

¹³ J. X. Yin, S. S. Zhang, G. Q. Chang, Q. Wang, S. S. Tsirkin, Z. Guguchia, B. Lian, H. B. Zhou, K. Jiang, I. Belopolski, N. Shumiya, D. Multer, M. Litskevich, T. A. Cochran, H. Lin, Z. Q. Wang, T. Neupert, S. Jia, H. C. Lei, and M. Z. Hasan, *Nat. Phys.* **15**, 443 (2019).

¹⁴ R. Yang, T. Zhang, L. Zhou, Y. Dai, Z. Liao, H. Weng, and X. Qiu, *Phys. Rev. Lett.* **124**, 077403 (2020).

¹⁵ Y. Okamura, S. Minami, Y. Kato, Y. Fujishiro, Y. Kaneko, J. Ikeda, J. Muramoto, R. Kaneko, K. Ueda, V. Kocsis, N. Kanazawa, Y. Taguchi, T. Koretsune, K. Fujiwara, A. Tsukazaki, R. Arita, Y. Tokura, and Y. Takahashi, *Nat. Commun.* **11**, 4619 (2020).

¹⁶ Q. Xu, E. Liu, W. Shi, L. Muechler, J. Gayles, C. Felser, and Y. Sun, *Phys. Rev. B* **97**, 235416 (2018).

¹⁷ I. V. Solovyev, S. A. Nikolaev, A. V. Ushakov, V. Y. Irkhin, A. Tanaka, and S. V. Streltsov, *Phys. Rev. B* **105**, 014415 (2022).

¹⁸ Z. Guguchia, J. A. T. Verezhak, D. J. Gawryluk, S. S. Tsirkin, J. X. Yin, I. Belopolski, H. Zhou, G. Simutis, S. S. Zhang, T. A. Cochran, G. Chang, E. Pomjakushina, L. Keller, Z. Skrzeczowska, Q. Wang, H. C. Lei, R. Khasanov, A. Amato, S. Jia, T. Neupert, H. Luetkens, and M. Z. Hasan, *Nat. Commun.* **11**, 559 (2020).

¹⁹ J.-R. Soh, C. Yi, I. Zivkovic, N. Qureshi, A. Stunault, B. Ouladdiaf, J. A. Rodríguez-Velamazán, Y. Shi, H. M. Rønnow, and A. T. Boothroyd, *Phys. Rev. B* **105**, 094435 (2022).

²⁰ M. V. Klein, *Light Scattering in Solids III* (Springer-Verlag, Berlin, 1958) p. 121.

²¹ T. P. Devereaux, A. Virosztek, and A. Zawadowski, *Phys.*

- Rev. B **51**, 505 (1995).
- ²² H.-M. Eiter, P. Jaschke, R. Hackl, A. Bauer, M. Gangl, and C. Pfeleiderer, *Phys. Rev. B* **90**, 024411 (2014).
- ²³ D. Farina, G. De Filippis, A. S. Mishchenko, N. Nagaosa, J.-A. Yang, D. Reznik, T. Wolf, and V. Cataudella, *Phys. Rev. B* **98**, 121104 (2018).
- ²⁴ R. Yang, Y. Dai, B. Xu, W. Zhang, Z. Qiu, Q. Sui, C. C. Homes, and X. Qiu, *Phys. Rev. B* **95**, 064506 (2017).
- ²⁵ B. Xu, Y. M. Dai, L. X. Zhao, K. Wang, R. Yang, W. Zhang, J. Y. Liu, H. Xiao, G. F. Chen, S. A. Trugman, J. X. Zhu, A. J. Taylor, D. A. Yarotski, R. P. Prasankumar, and X. G. Qiu, *Nat. Commun.* **8**, 14933 (2017).
- ²⁶ G. Breit and E. Wigner, *Phys. Rev.* **49**, 519 (1936).
- ²⁷ U. Fano, *Phys. Rev.* **124**, 1866 (1961).
- ²⁸ A. B. Kuzmenko, L. Benfatto, E. Cappelluti, I. Crassee, D. van der Marel, P. Blake, K. S. Novoselov, and A. K. Geim, *Phys. Rev. Lett.* **103**, 116804 (2009).
- ²⁹ A. H. Castro Neto and F. Guinea, *Phys. Rev. B* **75**, 045404 (2007).
- ³⁰ Z. Li, C. H. Lui, E. Cappelluti, L. Benfatto, K. F. Mak, G. L. Carr, J. Shan, and T. F. Heinz, *Phys. Rev. Lett.* **108**, 156801 (2012).
- ³¹ K. Zhang, T. Wang, X. Pang, F. Han, S.-L. Shang, N. T. Hung, Z.-K. Liu, M. Li, R. Saito, and S. Huang, *Phys. Rev. B* **102**, 235162 (2020).
- ³² T. P. Devereaux and R. Hackl, *Rev. Mod. Phys.* **79**, 175 (2007).
- ³³ G. Kresse and J. Hafner, *Phys. Rev. B* **47**, 558 (1993).
- ³⁴ G. Kresse and J. Furthmüller, *Comput. Mater. Sci.* **6**, 15 (1996).
- ³⁵ J. P. Perdew, K. Burke, and M. Ernzerhof, *Phys. Rev. Lett.* **77**, 3865 (1996).
- ³⁶ A. Togo, L. Chaput, T. Tadano, and I. Tanaka, *J. Phys. Condens. Matter* **35**, 353001 (2023).
- ³⁷ A. Togo, *J. Phys. Soc. Jpn.* **92**, 012001 (2023).
- ³⁸ R. Cohen, W. Pickett, and H. Krakauer, *Phys. Rev. Lett.* **64**, 2575 (1990).
- ³⁹ K. Tanaka, T. Nishihara, A. Takakura, Y. Segawa, K. Matsuda, and Y. Miyauchi, *J. Raman Spectrosc.* **54**, 93 (2023).
- ⁴⁰ C. Postmus, J. R. Ferraro, and S. S. Mitra, *Phys. Rev.* **174**, 983 (1968).
- ⁴¹ P. G. Klemens, *Phys. Rev.* **148**, 845 (1966).
- ⁴² J. Kosztin and A. Zawadowski, *Solid State Commun.* **78**, 1029 (1991).
- ⁴³ J. K. Freericks, T. P. Devereaux, M. Moraghebi, and S. L. Cooper, *Phys. Rev. Lett.* **94**, 216401 (2005).
- ⁴⁴ A. Nag, Y. Peng, J. Li, S. Agrestini, H. C. Robarts, M. García-Fernández, A. C. Walters, Q. Wang, Q. Yin, H. Lei, Z. Yin, and K.-J. Zhou, *Nat. Commun.* **13**, 7317 (2022).
- ⁴⁵ D. F. Liu, Q. N. Xu, E. K. Liu, J. L. Shen, C. C. Le, Y. W. Li, D. Pei, A. J. Liang, P. Dudin, T. K. Kim, C. Cacho, Y. F. Xu, Y. Sun, L. X. Yang, Z. K. Liu, C. Felser, S. S. P. Parkin, and Y. L. Chen, *Phys. Rev. B* **104**, 205140 (2021).
- ⁴⁶ C. Liu, J. Shen, J. Gao, C. Yi, D. Liu, T. Xie, L. Yang, S. Danilkin, G. Deng, W. Wang, S. Li, Y. Shi, H. Weng, E. Liu, and H. Luo, *Sci. China-Phys., Mech. Astron.* **64**, 217062 (2020).
- ⁴⁷ F. Pollmann, P. Fulde, and K. Shtengel, *Phys. Rev. Lett.* **100**, 136404 (2008).